

SYNTHETIC BIOLOGY

Engineering synthetic phosphorylation signaling networks in human cells

Xiaoyu Yang^{1,2,3}, Jason W. Rocks⁴, Kaiyi Jiang^{1†}, Andrew J. Walters^{1,3,5,6}, Kshitij Rai^{1,3}, Jing Liu¹, Jason Nguyen¹, Scott D. Olson⁶, Pankaj Mehta^{4,7,8}, James J. Collins^{9,10,11}, Nichole M. Daringer^{12*}, Caleb J. Bashor^{1,3,13*}

Protein phosphorylation signaling networks have a central role in how cells sense and respond to their environment. We engineered artificial phosphorylation networks in which reversible enzymatic phosphorylation cycles were assembled from modular protein domain parts and wired together to create synthetic phosphorylation circuits in human cells. Our design scheme enabled model-guided tuning of circuit function and the ability to make diverse network connections; synthetic phosphorylation circuits can be coupled to upstream cell surface receptors to enable fast-timescale sensing of extracellular ligands, and downstream connections can regulate gene expression. We engineered cell-based cytokine controllers that dynamically sense and suppress activated T cells. Our work introduces a generalizable approach that allows the design of signaling circuits that enable user-defined sense-and-respond function for diverse biosensing and therapeutic applications.

Cells universally use protein phosphorylation signaling networks to adapt to chemical and physical cues from their external environment. In metazoan cells, these networks consist of multilayered pathways that rapidly and reversibly convert signals detected by cell surface receptors into diverse responses such as cell movement, secretion, metabolism, and gene expression (1). The ability to design artificial phospho-signaling circuits that exhibit native-like signaling behavior, yet can be programmed with custom-defined input-output connectivity, could be used to create powerful biotechnology (2), including human cell-based therapeutics that autonomously sense and respond to specific physiological signals or disease markers on a fast timescale (3, 4).

Despite this potential, engineering of phospho-signaling circuits has lagged behind that of genetic circuits (5), for which advances in both microorganismal and mammalian settings have been enabled by design frameworks that leverage the intrinsic modularity of promoters and

coding regions (6), as well as carefully benchmarked sets of genetic parts (7, 8)—features that have facilitated scaling of circuit complexity and fine tuning of circuit behavior with predictive quantitative models (9, 10). Progress to date in engineering phospho-signaling circuits has included development of two-component phosphorylation pathways as programmable sense-and-respond modules in bacteria (11–13) and mammalian cells (14–16) and complex fast-timescale phosphorylation circuitry in yeast (17–19). In human cells, rewiring of native phospho-signaling networks has been used to create compact therapeutic programs (20) and sense-and-respond circuits that connect surface receptors to transcriptional outputs (21, 22). We sought to facilitate the de novo design of multilayered synthetic phosphorylation circuitry in human cells with programmable input-output connectivity and signal processing.

To establish such a framework, we emulated fundamental design features of native phospho-signaling networks, which are organized as sets of interlinked phosphorylation cycles comprising kinase and phosphatase activities that mutually act on a protein substrate (23, 24) (Fig. 1A). Changes in cycle equilibrium occur rapidly in response to input signals and are quickly reversed upon input removal, enabling cells to adapt to environmental changes on timescales of seconds to minutes. These features motivated us to design tunable, interconnectable phosphorylation cycles as elementary units for constructing synthetic signaling circuits. To accomplish this, we took advantage of the intrinsic structural modularity of signaling proteins, which are typically composed of discrete domains that either carry out catalytic function (for example, kinase or phosphatase domains) or specify interactions with other signaling components [for example, PDZ or Src homology 3 (SH3) domains] (25). The recombination of

catalytic and interaction domains is thought to allow rewiring signaling network connectivity during evolution (26) and has proved to be a versatile tool for engineering synthetic signaling network linkages (27) to create pathways with altered input-output relationships (28) or to introduce new information processing function (20, 29). We reasoned that orthogonal interaction domains could be used to mutually direct kinase and phosphatase domains to act on protein substrate targets, establishing synthetic cycles of phosphorylation and dephosphorylation that operate separately from native signaling networks.

To validate this design strategy, we developed a protein domain part set that included engineered catalytic domains derived from components of immune phosphotyrosine (pY) signaling pathways (figs. S1 and S2) (30). These proteins naturally use recruitment-dependent mechanisms of signaling activation and are weakly expressed in most nonimmune cell types (30). As an initial test, we fused various pY kinase domains (fig. S3) to leucine zippers (LZs)—small, highly specific heterodimerizing protein interaction domains with tunable interaction affinities (31)—to create synthetically targeted kinases (synKins) (fig. S4). Synthetic substrate proteins (synSubs) for the synKins were constructed by fusing cognate LZs with ITAMs (immunoreceptor tyrosine-based activation motifs), conserved pY motifs involved in immune signaling pathway activation (Fig. 1B and fig. S4) (32). Plasmid constructs encoding pairs of epitope-tagged synKins and synSubs (fig. S4) were transfected into human embryonic kidney (HEK) 293T cells, and multicolor flow cytometry was used to simultaneously measure component expression (staining of epitopes) and synSub phosphorylation (staining of phosphorylated ITAMs) in single cells (fig. S5). To optimize synKin function, we tested numerous kinase domain boundaries and point mutations (fig. S6). We identified variants that showed strong expression and demonstrated phosphorylation activity toward synSub that was highly dependent on LZ-mediated kinase domain recruitment, as evidenced by nonbinding, catalytically inactive, and unrecruited (noncognate LZ) controls all showing little or no phosphorylation (Fig. 1B, right, and fig. S7, A to C). We observed minimal cross-talk of these components with host cell machinery: Expression of synKin showed limited nonspecific Y phosphorylation, and synSub phosphorylation in the absence of synKin expression was negligible (fig. S7, B and C). Further, we found that expression of our proteins showed no major limiting effect on cell viability or growth rate (fig. S7D).

We tested whether we could tune the activity of synKin toward synSub by altering the molecular properties of the domain parts. We constructed several sets of synKin variants: LZ

¹Department of Bioengineering, Rice University, Houston, TX, USA. ²Graduate Program in Systems, Synthetic and Physical Biology, Rice University, Houston, TX, USA. ³Rice Synthetic Biology Institute, Rice University, Houston, TX, USA.

⁴Department of Physics, Boston University, Boston, MA, USA. ⁵Graduate Program in Bioengineering, Rice University, Houston, TX, USA. ⁶Department of Pediatric Surgery, McGovern Medical School, University of Texas Health Science Center at Houston, Houston, TX, USA. ⁷Biological Design Center, Boston University, Boston, MA, USA. ⁸Faculty of Computing and Data Science, Boston University, Boston, MA, USA. ⁹Institute for Medical Engineering and Science, Department of Biological Engineering, and Synthetic Biology Center, Massachusetts Institute of Technology, Cambridge, MA, USA. ¹⁰Broad Institute of MIT and Harvard, Cambridge, MA, USA. ¹¹Wyss Institute for Biologically Inspired Engineering, Harvard University, Boston, MA, USA. ¹²Department of Biomedical Engineering, Rowan University, Glassboro, NJ, USA.

¹³Department of Biosciences, Rice University, Houston, TX, USA. *Corresponding author. Email: caleb.bashor@rice.edu (C.J.B.); daringer@rowan.edu (N.M.D.)

[†]Present address: Department of Biological Engineering, Massachusetts Institute of Technology, Cambridge, MA, USA.

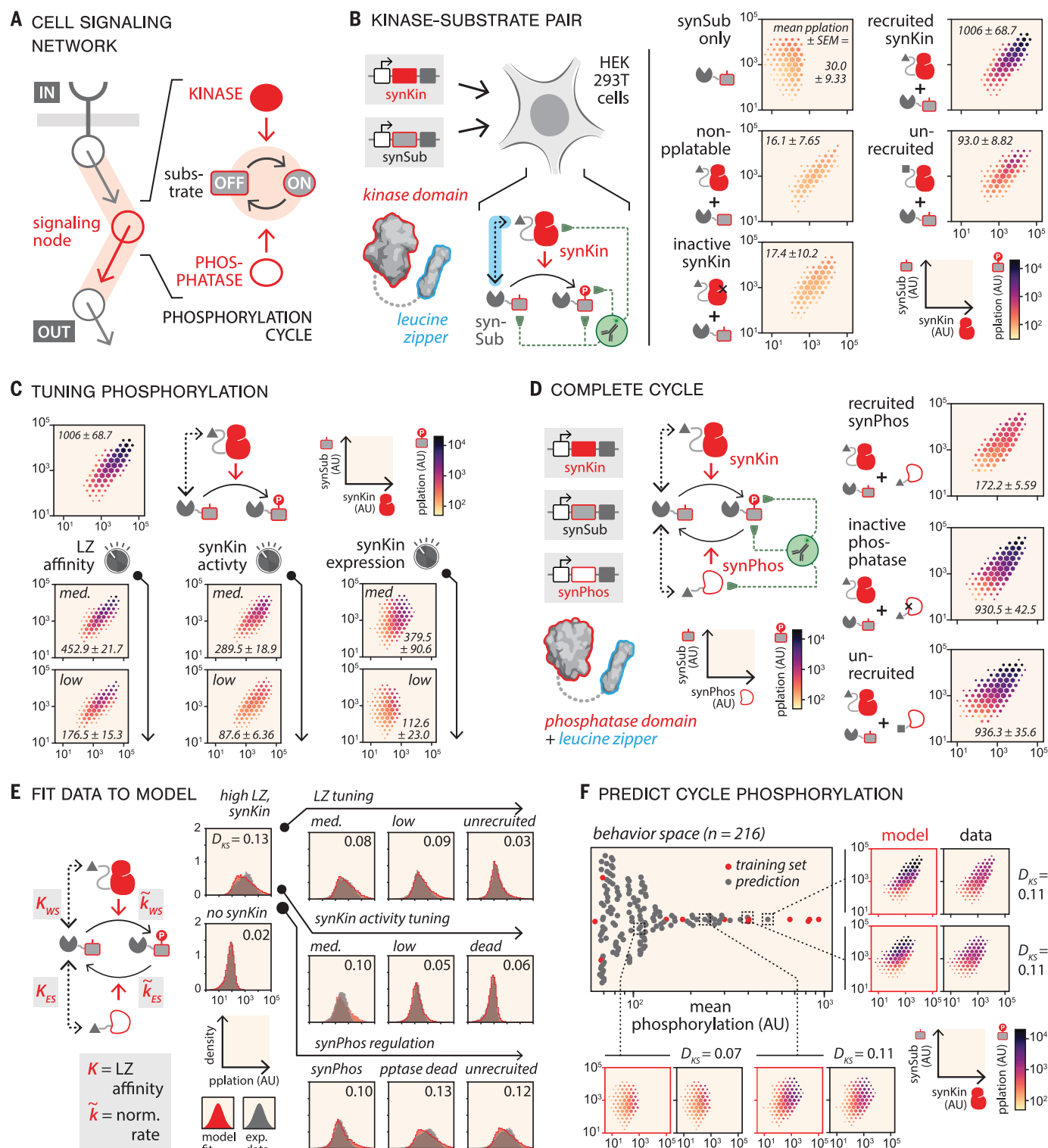


Fig. 1. Building and tuning synthetic phosphorylation cycles in human cells. (A) Phosphorylation cycles, in which kinase and phosphatase activities mutually regulate (red arrows) phosphorylation equilibrium (black arrows) of a substrate, are fundamental units that make up phospho-signaling networks. (B) Engineering synthetic kinase (synKin) and substrate (synSub) pairs. Plasmids (gray rectangles) encoding synKin and synSub proteins are transfected into HEK293T cells and measured for expression and phosphorylation with immunofluorescence flow cytometry (green dotted lines) after 36 hours. Leucine zippers (LZs) mediate interactions (cyan dashed line) between synKin and

synSub proteins (left). Expression and phosphorylation data for synKin-synSub allele combinations are shown at right as hexagonal-hit-and-heat (HHH) plots. Through the whole study, the expression space was uniformly binned into grids; the hexagon size indicates the cell counts in each bin, the largest hexagon size indicates the highest cell density, and the smallest hexagon size indicates the lowest density, with hexagon sizes in between indicating log10-normalized cell counts proportionally (fig. S5). Values associated with HHH plots are mean phosphorylation (AU, arbitrary units) \pm SEM ($n = 3$ biological replicates). (C) Tuning synSub phosphorylation. Phosphorylation was measured for synKin-synSub

compositions that feature parts that tune LZ binding affinity, synKin expression level, and synKin activity. (Top) The behavior of the default synKin-synSub from (B) for comparison. Numbers are associated with HHH plots, mean phosphorylation (AU) \pm SEM ($n = 3$ biological replicates). (D) Complete synthetic phosphorylation cycle. (Left) LZ-recruited synPhos dephosphorylates synSub. (Right) Values adjacent to HHH plots of synPhos variants indicate mean phosphorylation (AU) \pm SEM ($n = 3$ biological replicates). (E) Modeling synthetic phosphorylation cycle equilibrium. (Left) LZ interactions [K_{WS} , synKin-synSub affinity (W, writer; S, substrate); K_{ES} , synPhos-synSub affinity (E, eraser; S, substrate)] and component activity (\bar{k}_{WS} , normalized phosphorylation rate; \bar{k}_{ES} , normalized dephosphorylation rate) of the cycle (model description is available in the supplementary text). Phosphorylation cycle data from (B) to (D) were used for fitting. Model-predicted

phosphorylation distributions (red) are plotted against experimentally measured distributions (gray). Kolmogorov-Smirnov divergence (D_{KS}) values comparing model with experiment are shown for each plot. norm., normalized. (F) Model-predicted phosphorylation cycle behavior space. The beeswarm plot shows phosphorylation values for predicted (gray dots) and training (red dots) part compositions (216 total). HHH plots for compositions from across design space (indicated with black dotted lines) compare predicted phosphorylation (red borders) and measured phosphorylation (black borders). Compositions of highlighted circuits are identical to synPhos composition in (D) (strong synKin and synPhos LZ, strong synKin and synPhos activity, and strong synKin and synPhos expression) except for the following: bottom left, low synKin expression, dead synPhos; bottom middle, medium synKin expression, weak synPhos LZ; top right, low synPhos; bottom right, weak synPhos activity, medium synKin LZ.

sequence variants were introduced to tune binding affinity to synSub (37); catalytic turnover rate was adjusted with previously reported pY kinase domain active site mutations (fig. S4) (33); and expression level was tuned by introducing Kozak sequence variants to synKin expression constructs, resulting in differential rates of protein translation (34). When we tested each synKin part set, we observed modulation of synSub phosphorylation across a 10- to 20-fold range (Fig. 1C). To create complete cycles of reversible synSub phosphorylation, we developed synthetically targeted pY phosphatases (synPhos). We took an approach similar to what we used for the synKins, identifying domain variants derived from pY phosphatases involved in immune signaling (figs. S8 to S9) (35) and fusing them to the same LZ species as that with the synKin. When coexpressed with a synKin-synSub pair, synPhos dephosphorylated synSub in a recruitment-dependent and phosphatase activity-dependent manner (Fig. 1D). Taken together, these results validate our design strategy for constructing synthetic phosphorylation cycles and demonstrate that a simple part set that consists of catalytic and interactions domain variants can be used to rationally control intracellular phosphorylation equilibrium.

We developed a model to quantitatively describe the relationship between phosphorylation cycle equilibrium and part biophysical properties. To achieve this, we first converted single-cell fluorescence values into stoichiometric equivalents for all phosphorylation cycles depicted in Fig. 1, B to D, by normalizing different color fluorophores to an enhanced green fluorescent protein (EGFP) reference (figs. S10 and S11). These transformed data were then fit to a nonequilibrium thermodynamic model (Fig. 1E and fig. S12) to obtain part-specific parameters for LZ variant interaction affinities (K_{WS} , K_{ES}) and catalytic turnover rates of synKin and synPhos variants (\bar{k}_{WS} , \bar{k}_{ES}) (fig. S12). The parameterized model was then used to predict phosphorylation states for all part combinations within our design space ($n = 216$ total compositions) (Fig. 1F and fig. S13). To validate these predictions, we constructed and

measured compositions from across the predicted behavior distribution; all showed excellent overall agreement with the model (Fig. 1F), demonstrating that the functional modularity inherent in our design scheme lends itself to prediction of regulated phosphorylation behavior based on individual parts properties. Last, we used the model to analyze our part set for compositions that could undergo sharp, ultrasensitive transition in phosphorylation upon changes in component activity, expression levels, and LZ affinity (fig. S14). From this analysis, we determined that the behavior for the majority of compositions in our part design space fall in a linear regime, although tuning to higher sensitivity is possible by using higher synKin LZ affinity, lower synPhos LZ affinity, and higher synSub expression.

Native signaling networks convert protein phosphorylation into molecular outputs through various mechanisms (36), including allosteric regulation of protein activity, changes in protein localization and stability, and formation of new protein-protein interactions. In the latter case, phospho-specific binding domains recognize phosphorylated substrate motifs, forming interactions that facilitate downstream signaling. To form circuit connections between phosphorylation cycles, we used engineered SH2 domains, which bind to pY-containing motifs and are conserved among metazoans (Fig. 2A) (37). We used a transcriptional reporter (fig. S15, A and B) to not only validate synKin activity-dependent SH2-pY motif interactions but also to identify part sets with orthogonal interaction specificities (fig. S15D): Tandem SH2 (tSH2) domains and an engineered multivalent SH2 respectively bound synKin-phosphorylated ITAMs (fig. S15C) (38) and a dual pY motif derived from the immune signaling protein SLP76 (SH2-domain-containing leukocyte protein of 76 kDa) (fig. S16A), with no observable cross-talk (fig. S16B).

To test whether these phospho-dependent interactions could be used to link two phosphorylation cycles together, we engineered a “phospho-couple” (PC) protein that integrates the functions of an upstream synSub and downstream synKin by fusing a kinase domain to

three substrate motifs and placing a rigid linker domain between them (fig. S17) to limit cis-phosphorylation (Fig. 2A, right, and fig. S17). This design facilitated sequential activation of phosphorylation cycles: When we expressed a four-protein system (upstream synKin, PC, synPhos, and downstream SH2-synSub) in HEK293T cells, phosphorylation of PC by the upstream synKin led to recruitment and phosphorylation of a downstream, tSH2-fused synSub (Fig. 2B). Sequential phosphorylation was dependent on upstream synKin recruitment, PC activity, and SH2-mediated recruitment, as well as 3 \times substrate motif valency (Fig. 2B, right).

One important systems-level property of native phosphorylation cascades is their ability to stoichiometrically amplify weak input signals into macroscopic cellular outputs (39). To determine whether our two-step circuit architecture could be tuned to maximize amplification of an upstream input, we expanded our quantitative model to fit data from Fig. 2B, obtaining part-specific parameters (fig. S18) that allowed behavior predictions across two-step circuit combinatorial design space ($n = 3456$ compositions) (Fig. 2C, left). We identified a region of behavior space with compositions predicted to show a >10 \times fold-change in downstream synSub phosphorylation upon addition of an upstream synKin ($n = 261$ compositions). Circuits from this high-gain region were enriched for features that are consistent with stoichiometric amplification, including a low PC:SH2-synSub ratio and strong synPhos activity (fig. S19). To validate model predictions, we selected several amplifier circuit compositions from this region to experimentally measure, demonstrating the general agreement of their behavior with model predictions (Fig. 2C, right). These results indicate that our part set and predictive modeling framework can be extended to guide the design of multiphosphorylation cycle networks with programmed signal-processing properties.

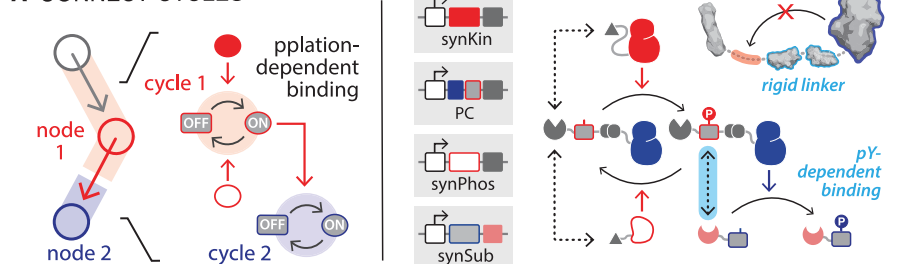
Having developed approaches for building, interconnecting, and predictively tuning synthetic phosphorylation cycles, we sought to engineer surface receptors that could couple extracellular ligand binding to changes in

Fig. 2. Building and tuning phosphorylation

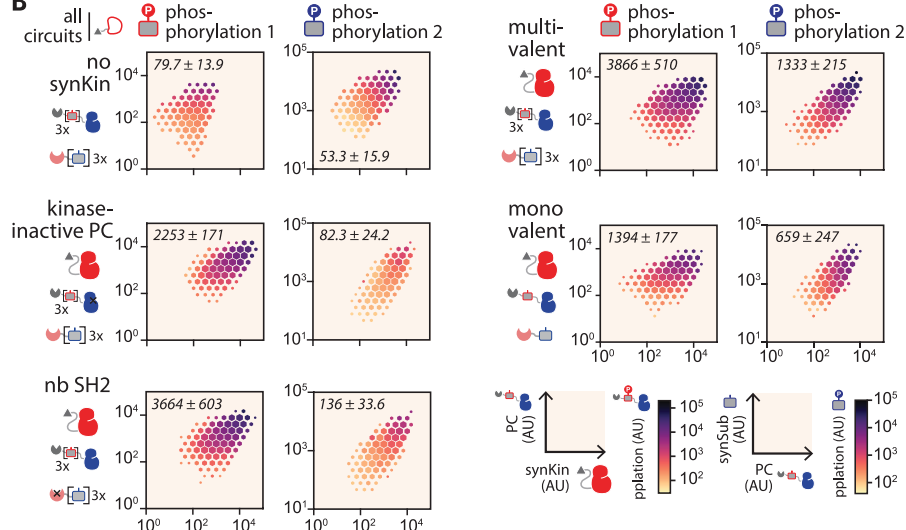
cycle networks. (A) Two-step phosphorylation cascade circuit. To create a synthetic phosphorylation network connection, an upstream cycle (red) can be coupled to a downstream cycle (blue) by using a phosphorylation-dependent interaction (left). The upstream synKin phosphorylates a “phospho-couple” (PC) protein, which functions as synSub for the upstream cycle and synKin for the downstream one (right). The PC contains a rigid linker domain (cyan outline) that prevents cis substrate motif phosphorylation while supporting SH2-mediated recruitment of a downstream substrate (cyan dashed line at top right). **(B)** Two-step circuit validation. HHH plots for PC (left column) and synSub (right column) phosphorylation are shown for various circuit compositions. All circuit compositions contain synPhos. Brackets indicate the number of ITAM motif repeats. Values in each plot are mean phosphorylation (AU) \pm SEM ($n = 3$ biological replicates). **(C)** Model-predicted circuit behavior space for two-step circuit. The modeling framework was used to fit steady-state phosphorylation of multivalent two-step circuits from (B) (fig. S18). Scatter plot shows predicted mean phosphorylation for compositions with (y axis) and without (x axis) upstream synKin. Red dots indicate training set compositions from fig. S18B; gray dots indicate model-predicted compositions (3456 total). Region of $>10\times$ fold-change (\pm synKin) is shown in cyan. Four high-gain circuits (indicated with black dotted lines) were constructed and tested for synSub phosphorylation. (Right) HHH plots for model-predicted (red border) and experimental measurements (black border) are shown. Compositions of highlighted circuits are identical with the multivalent composition in (B), except for the following: (1), medium PC kinase activity, high synPhos activity; (2), low PC expression; (3), high synKin expression, low PC expression; and (4), high PC expression, high synPhos expression. Values at the top of each plot indicate mean phosphorylation (AU) \pm SEM ($n = 3$ biological replicates). D_{KS} values are shown at the bottom of each experimental plot. Predicted (red) and experimentally measured (black) fold change values are shown at right of the plots.

phosphorylation cycle equilibrium (Fig. 3A, left). We constructed a pair of synthetic receptor scaffolds (figs. S20) that consisted of flexible intracellular and extracellular linker sequences and transmembrane helices. Kinase and LZ domains were appended to the cytoplasmic termini of the scaffolds, and FKBP (FK506 binding protein) and FRB* (FKBP-rapamycin-binding domain of mTOR kinase, K2095P)—domains that heterodimerize upon binding to

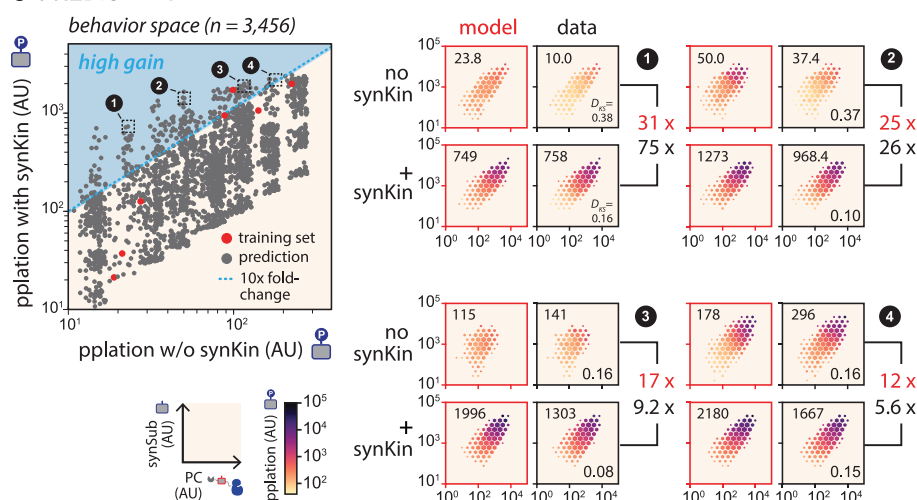
A CONNECT CYCLES



B



C PREDICT 2-STEP CIRCUIT PHOSPHORYLATION



the rapamycin analog AP21967 (40)—to their extracellular termini. This architecture should enable ligand-induced synSub phosphorylation as a result of receptor dimerization-enforced proximity between the synKin and LZ (Fig. 3A, right). After transfecting a four-protein system consisting of the receptor pair, synSub, and synPhos proteins, we observed a ~20-fold change in phosphorylation upon ligand addition. Circuit induction was dependent on both

LZ-mediated synSub recruitment and synKin activity. Additionally, we observed that elimination of synPhos activity resulted in a lower fold-change response (6.9 \times), demonstrating the importance of phosphorylation cycle reversibility for optimizing circuit performance (Fig. 3B). Last, the dose response profile for the circuit was highly linear [Hill coefficient (n_H) = 1.1].

To assess the timescale of activation for our receptor-mediated phospho-sensor circuit, we

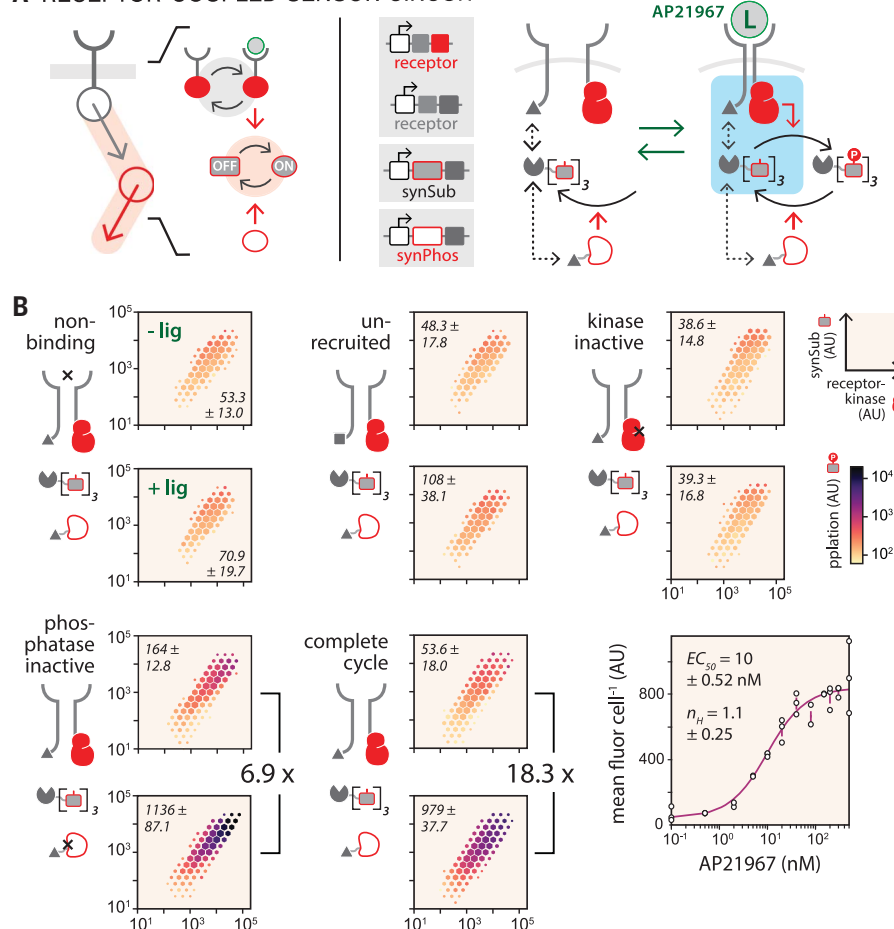
Fig. 3. Constructing receptor-coupled sensor circuits.

(A) Sensor circuit design. (Left) Reversible ligand binding to extracellular receptors triggers phosphorylation cycle activation. The circuit is encoded as four genes on three plasmids; it includes two receptor chains (FRB*-TM-kinase domain and FKBP-TM-LZ), a synSub with three motif repeats, and a synPhos. (Right) Dimerization of extracellular FRB* and FKBP domains induced by ligand (AP21967) triggers colocalization of receptor-appended kinase with synSub (cyan box), leading to phosphorylation.

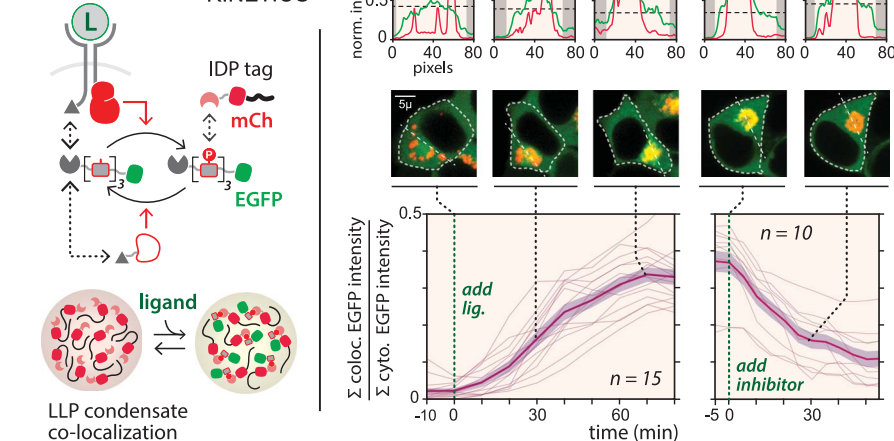
(B) Testing receptor-induced phosphorylation. HHH plots depict flow-cytometry data from sensor circuit compositions analyzed 12 hours after treatment with 200 nM ligand AP21967 (+ lig) or a carrier-only control (– lig). Values in each plot indicate mean phosphorylation (AU) ± SEM ($n = 3$ biological replicates). Phosphorylation fold-change values are next to each set of plots. (Bottom right) Dose response plot shows synSub phosphorylation as a function of ligand concentration. Individual triplicate measurements (circles) with mean ± SEM (error bars) are shown. Data were fitted (magenta line) to eq. S150 (supplementary materials) (n_H , Hill coefficient; EC_{50} , input at 50% activation).

(C) Measuring pathway activation by using a LLP condensate colocalization reporter. (Left) The reporter consists of EGFP-tagged synSub and an mCherry-tagged SH2 domain tagged with an intrinsically disordered protein (IDP); phosphorylation leads synSub-EGFP recruitment to condensates and EGFP-mCherry colocalization. For activation experiments, cells were cultured for 24 hours, and then time-lapse images were taken every 10 min after ligand addition over an 80-min time course to track pathway activation (left time course plot). For deactivation experiments, 200 nM ligand was added for 90 min followed by addition of the inhibitor imatinib mesylate (10 μ M), and then time-lapse images were taken every 5 min after inhibitor addition over a 60-min time course (right time course plot). Data are plotted as single-cell trajectories (thin pink lines) for activation ($n = 15$ cells) and deactivation ($n = 10$ cells), with mean values (thick pink line) ± SEM (shaded pink bands). (Middle right) For selected time points (0, 30, and 70 min for activation and 0 and 30 min for deactivation), images of EGFP and mCherry (false-colored green and red, respectively) are shown for representative single cells, with the cell boundaries (dotted white outlines) as determined with custom segmentation software. (Top right) Histograms show max-normalized EGFP and mCherry intensities along the straight white dashed lines drawn in images, and intensity is plotted for each channel in the same plot, with the black dashed line indicating max-normalized cytoplasmic EGFP intensity; shaded regions indicate outside the cytoplasm. Scale bars, 5 μ m.

A RECEPTOR-COUPLED SENSOR CIRCUIT



C CIRCUIT ACTIVATION KINETICS

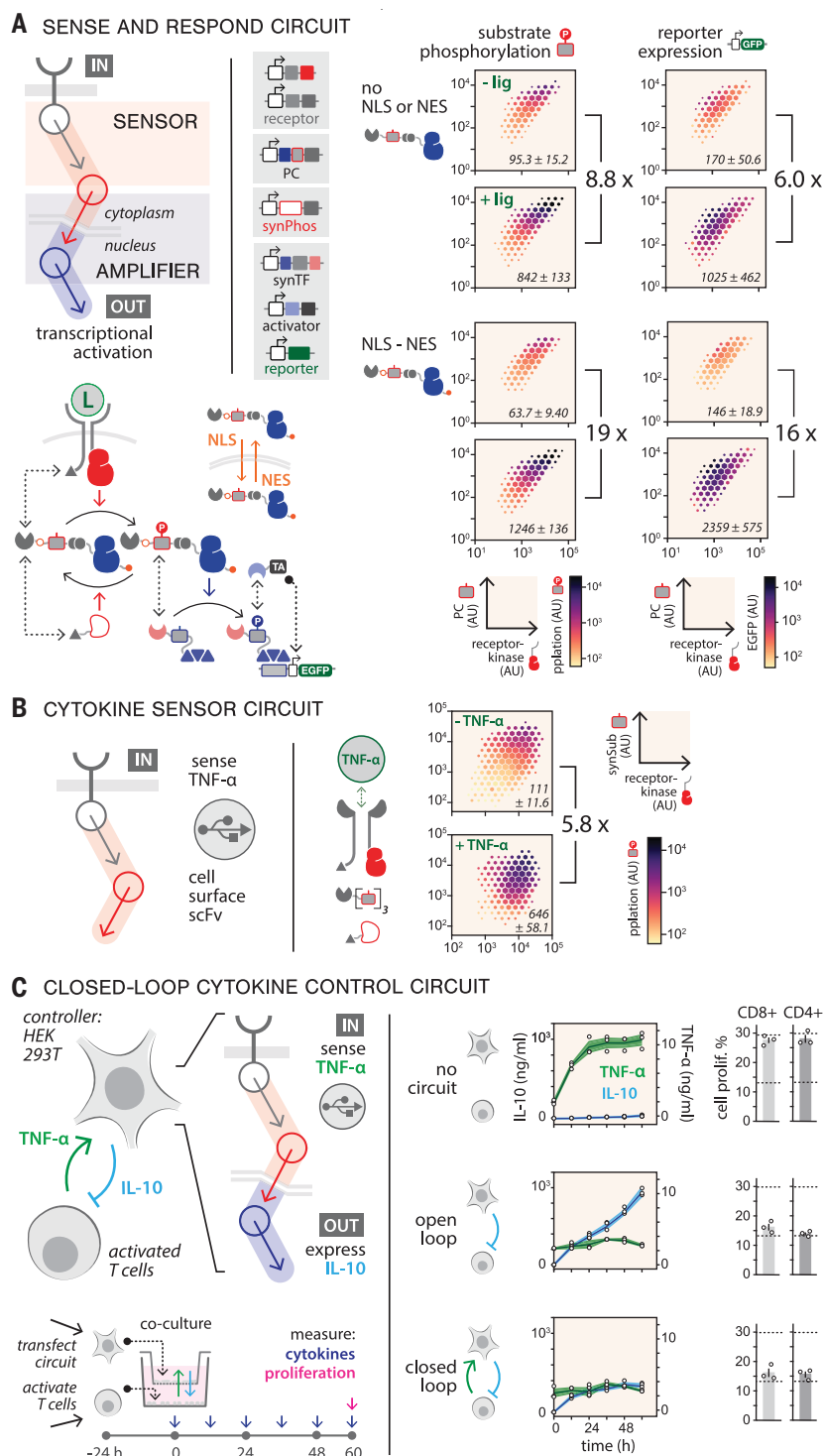


engineered a reporter system that allowed us to track in real time with fluorescence microscopy the accumulation of phosphorylated synSub (Fig. 3C). The reporter was created by fusing an SH2 domain and mCherry fluorescent protein to a tag derived from polar orga-

nizing protein Z (41), an intrinsically disordered protein that can sequester fused client proteins into cytoplasmically localized liquid-liquid phase (LLP) condensates (fig. S21A) (42). This enabled us to monitor circuit activation by quantifying the colocalization of EGFP-

fused synSub to the condensates as a proxy for phosphorylation (fig. S21, B and C, and movie S1). We detected EGFP-mCherry colocalization within 10 min after ligand addition, and steady state was reached after ~1 hour, whereas addition of a synKin inhibitor to the fully active

Fig. 4. Phosphorylation circuit-mediated closed-loop sense-and-response function. (A) Using phospho-signaling to connect extracellular sensing to transcriptional output. (Left) The phospho-sensor circuit (Fig. 3) was coupled to a two-step amplifier circuit (Fig. 2), which was in turn coupled to a phosphorylation-dependent transcriptional reporter module (fig. S19), yielding a membrane-to-nucleus signaling pathway. The PC is tagged with nuclear localization (NLS) and nuclear export signals (NES) to enable shuttling between the nucleus and cytoplasm. (Right) HHH plots for (left column) PC phosphorylation and (right column) EGFP expression are shown for cells \pm ligand for compositions with and without NLS or NES tags. Values in the plots indicate mean fluorescence (AU) \pm SEM ($n = 3$ biological replicates). Fold-change values are shown at right of each set of plots. (B) Cytokine sensor circuit. Receptor chains in Fig. 3 are appended to (single-chain variable fragments) scFvs that bind to human TNF- α . TNF- α binding induced synSub phosphorylation. (Right) HHH plots depict flow cytometry data analyzed 12 hours after treatment with 20 ng/ml TNF- α (+ lig) or a carrier-only control (– lig). Values in each plot indicate mean phosphorylation (AU) \pm SEM ($n = 3$ biological replicates). (C) Engineering a phospho-signaling pathway for closed-loop therapeutic control. (Top left) HEK293T cells expressing a circuit that can sense TNF- α (green arrow) and respond by secreting IL-10 (blue arrow) are (bottom left) placed in transwell coculture with activated T cells for 60 hours, with media collected every 12 hours to measure cytokine levels. T cell proliferation was assessed by means of EdU assay at 60 hours. TNF- α and IL-10 time courses are shown for empty HEK293T cells (no circuit), constitutive IL-10 expression driven by a nonreceptor synKin driving phosphorylation of 2-step cascade (open loop), and the sense-and-respond circuit (closed loop). (Middle) Each circle indicates a different PBMC replicate (black line, mean values; shaded regions, \pm SEM). Measurements of CD4 $^{+}$ and CD8 $^{+}$ proliferation, with circles indicating data from three PBMC biological replicates. Error bars indicate mean values \pm SEM [$n = 3$ measurements; top dashed line, proliferation (maximum EdU signal) of activated T cells alone with no HEK293T cell; bottom dashed line, proliferation of activated T cells inhibited with 500 ng/ml IL-10 (minimum EdU signal)].



pathway led to rapid synPhos-dependent delocalization (Fig. 3C and movie S2). In a circuit in which synPhos was absent, delocalization occurred $>10\times$ slower, demonstrating that synPhos is critical for rapid circuit reversibility (fig. S22A). Fitting these data to a dynamic model (fig. S22B) yielded circuit activation and deactivation half-times of 28.8 and 22.8 min, respectively—rapid dynamics similar to those

measured for JAK/STAT (Janus kinase/signal transducer and activator of transcription) (43) and TGF- β (transforming growth factor- β) cytokine signaling pathway (fig. S22C) (44).

We tested whether we could combine our phospho-sensor and two-step amplifier modules to create a sense-and-respond circuit that would convert an extracellular input signal into expression of a transgene (Fig. 4A, left,

and fig. S23A). To promote membrane-to-nucleus signal propagation, we selected an amplifier composition [Fig. 2C, (2)] that showed both high gain and high downstream phosphorylation, and we appended nuclear localization sequence (NLS) and nuclear exporting sequence (NES) to the PC to promote shuttling between the cytoplasm and nucleus. Regulation of transcriptional activation was implemented

by fusing the second substrate to a synthetic zinc finger transcription factor (synTF) (10) to facilitate phospho-dependent recruitment of an SH2-fused transcriptional activation domain (TAD), resulting in initiation of EGFP reporter expression. We tested this six-protein, seven-gene circuit in HEK293T cells and observed PC phosphorylation (19× fold-change) and EGFP expression (16× fold-change) in response to ligand addition (Fig. 4A, right). Circuit designs not tagged with a NLS or NES (fig. S23B) and lower-gain circuit designs (fig. S24A) showed <10× fold-change, underscoring the importance of shuttling and amplification as circuit design features. The circuit also demonstrated a linear dose-response profile ($n_H = 0.97$) (fig. S24B).

As a demonstration of the translational potential of our framework, we engineered a circuit that senses tumor necrosis factor- α (TNF- α)—a cytokine secreted by T cells that drives adverse inflammatory response—and responds by secreting interleukin 10 (IL-10), a cytokine that inhibits T cell activation, proliferation, and TNF- α production but has toxic side effects that limit its clinical utility (45). This circuit could establish an anti-inflammatory control loop that suppresses T cell activation while maintaining low concentrations of both cytokines. We tested this by reconfiguring the sense-and-respond circuit shown in Fig. 4A; we appended single-chain antibody fragments (scFvs) that recognize TNF- α to the receptors (Fig. 4B and fig. S25) and replaced the EGFP reporter with IL-10. HEK293T cells containing this circuit were introduced into a transwell coculture with CD3- and CD28-activated human peripheral blood mononuclear cells (PBMCs), and cytokine production and T cell proliferation were assessed across a 60-hour time course (Fig. 4C, left). Cocultures containing cells with no circuit showed rapid accumulation of TNF- α and robust T cell proliferation, whereas cells containing a circuit driving constitutive IL-10 expression (open-loop composition) inhibited TNF- α secretion and T cell proliferation (Fig. 4C, right, and fig. S26). Cells containing the sense-and-respond circuit (closed-loop composition) also suppressed T cell proliferation but reached low steady-state concentrations of both TNF- α and IL-10 after ~12 hours. As indicated by modeling the dynamics of this system (fig. S27), this rapid setpoint convergence is likely dependent on the fast activation and deactivation rates of our phospho-signaling circuit and may not be achievable with circuits that use molecular mechanisms that operate on slower timescales (figs. S27 and S28).

We engineered synthetic phospho-signaling circuits using a simple design logic in which phosphorylation cycles are used as building blocks, and circuit connectivity and information flow are defined through programmed protein-protein interactions. Our design framework enabled predictive tuning of circuit

behavior and the use of nonequilibrium thermodynamic modeling to guide circuit design. Although the part set we used in this study to demonstrate the practicability of our design scheme consisted largely of domains and motifs repurposed from native human immune signaling, our framework should facilitate incorporation of domains drawn from other sources or generated through computational design (46). Catalytic domains could be engineered to enhance circuit performance through activity tuning or by introducing allosteric regulation. Because the functional specificities of our components are determined by recruitment, scaling to greater circuit complexity could be enabled by simply expanding the number of orthogonal interaction domains in our part set. This could facilitate the construction of circuit topologies that carry out advanced signal processing functions, such as Boolean logic enabled through multisite phosphorylation, feedback connections that tune circuit dynamics or introduce ultrasensitivity (47), or multi-input-output circuits that can perceive and compute internal or external states (48).

Last, because our circuits are posttranslational and signal rapidly and reversibly, they can potentially support a broad array of cell-based diagnostic and therapeutic applications that require sensing of minute-scale physiological or pathological events (4). The plug-and-play configurability of our circuits should enable their coupling to diverse receptor inputs capable of sensing small molecules, bioactive factors, or disease markers (49). Because of their temporal responsiveness, the circuits may complement or offer advantages over other highly programmable circuit design schemes that signal through slower-turnover molecular mechanisms (such as transcription or proteolysis) (50). Additionally, because our circuits operate in parallel to native signaling pathways, they offer opportunities for programming signal-processing functions that are not possible for signaling circuits that harness native components to propagate signal. Furthermore, because they can be configured with human-derived protein domains and are relatively compact, circuits constructed by using our design framework are likely to have low immunogenicity (fig. S29) and could potentially be delivered to clinically relevant cell types (fig. S30) to enable therapeutic sense-and-respond function.

REFERENCES AND NOTES

1. T. Pawson, J. D. Scott, *Trends Biochem. Sci.* **30**, 286–290 (2005).
2. W. A. Lim, *Nat. Rev. Mol. Cell Biol.* **11**, 393–403 (2010).
3. R. Kojima, D. Aubel, M. Fussenegger, *Cell. Mol. Life Sci.* **77**, 3567–3581 (2020).
4. C. J. Bashor, I. B. Hilton, H. Bandukwala, D. M. Smith, O. Veiseth, *Nat. Rev. Drug Discov.* **21**, 655–675 (2022).
5. D. E. Cameron, C. J. Bashor, J. J. Collins, *Nat. Rev. Microbiol.* **12**, 381–390 (2014).
6. C. J. Bashor, J. J. Collins, *Annu. Rev. Biophys.* **47**, 399–423 (2018).

7. A. S. Khalil et al., *Cell* **150**, 647–658 (2012).
8. C. A. Voigt, *Curr. Opin. Biotechnol.* **17**, 548–557 (2006).
9. A. A. Nielsen et al., *Science* **352**, aac7341 (2016).
10. C. J. Bashor et al., *Science* **364**, 593–597 (2019).
11. J. M. Skerker et al., *Cell* **133**, 1043–1054 (2008).
12. W. R. Whitaker, S. A. Davis, A. P. Arkin, J. E. Dueber, *Proc. Natl. Acad. Sci. U.S.A.* **109**, 18090–18095 (2012).
13. S. R. Schmidl et al., *Nat. Chem. Biol.* **15**, 690–698 (2019).
14. A. Mazé, Y. Benenson, *Nat. Chem. Biol.* **16**, 179–187 (2020).
15. L. Scheller et al., *Nat. Commun.* **11**, 3085 (2020).
16. R. D. Jones et al., *Nat. Commun.* **13**, 1720 (2022).
17. D. Mishra, P. M. Rivera, A. Lin, D. Del Vecchio, R. Weiss, *Nat. Biotechnol.* **32**, 1268–1275 (2014).
18. D. Mishra et al., *Science* **373**, eaav0780 (2021).
19. R. M. Gordley et al., *Proc. Natl. Acad. Sci. U.S.A.* **113**, 13528–13533 (2016).
20. H. K. Chung et al., *Science* **364**, eaat6982 (2019).
21. L. Schukur, B. Geering, G. Charpin-El Hamri, M. Fussenegger, *Sci. Transl. Med.* **7**, 318ra201 (2015).
22. K. Krawczyk, L. Scheller, H. Kim, M. Fussenegger, *Nat. Commun.* **11**, 608 (2020).
23. A. Goldbeter, D. E. Koshland Jr., *Proc. Natl. Acad. Sci. U.S.A.* **78**, 6840–6844 (1981).
24. D. Bray, *Nature* **376**, 307–312 (1995).
25. T. Pawson, P. Nash, *Genes Dev.* **14**, 1027–1047 (2000).
26. R. P. Bhattacharyya, A. Reményi, B. J. Yeh, W. A. Lim, *Annu. Rev. Biochem.* **75**, 655–680 (2006).
27. Z. Chen, M. B. Elowitz, *Cell* **184**, 2284–2301 (2021).
28. S. H. Park, A. Zarrinpar, W. A. Lim, *Science* **299**, 1061–1064 (2003).
29. C. J. Bashor, N. C. Helman, S. Yan, W. A. Lim, *Science* **319**, 1539–1543 (2008).
30. A. H. Courtney, W. L. Lo, A. Weiss, *Trends Biochem. Sci.* **43**, 108–123 (2018).
31. A. Acharya, S. B. Rudinov, J. Gal, J. R. Moll, C. Vinson, *Biochemistry* **41**, 14122–14131 (2002).
32. D. M. Underhill, H. S. Goodridge, *Trends Immunol.* **28**, 66–73 (2007).
33. Y. Cui, G. Sun, *Protein Sci.* **28**, 533–542 (2019).
34. J. P. Ferreira, K. W. Overton, C. L. Wang, *Proc. Natl. Acad. Sci. U.S.A.* **110**, 11284–11289 (2013).
35. L. Tautz, D. A. Critton, S. Grotegut, *Methods Mol. Biol.* **1053**, 179–221 (2013).
36. J. A. Ubersax, J. E. Ferrell Jr., *Nat. Rev. Mol. Cell Biol.* **8**, 530–541 (2007).
37. T. Pawson, *Cell* **116**, 191–203 (2004).
38. E. A. Ottinger, M. C. Botfield, S. E. Shoelson, *J. Biol. Chem.* **273**, 729–735 (1998).
39. P. B. Detwiler, S. Ramanathan, A. Sengupta, B. I. Shraiman, *Biophys. J.* **79**, 2801–2817 (2000).
40. B. Z. Stanton, E. J. Chory, G. R. Crabtree, *Science* **359**, eaao5902 (2018).
41. G. Ebersbach, A. Briegel, G. J. Jensen, C. Jacobs-Wagner, *Cell* **134**, 956–968 (2008).
42. S. Boeynaems et al., *Trends Cell Biol.* **28**, 420–435 (2018).
43. H. Kiu, S. E. Nicholson, *Growth Factors* **30**, 88–106 (2012).
44. B. Labibi, M. Bashkurov, J. L. Wrana, L. Attisano, *iScience* **23**, 101416 (2020).
45. A. Saxena et al., *Cytokine* **74**, 27–34 (2015).
46. N. B. Woodall et al., *Nat. Struct. Mol. Biol.* **28**, 762–770 (2021).
47. J. E. Ferrell Jr., S. H. Ha, *Trends Biochem. Sci.* **39**, 612–618 (2014).
48. Z. Chen et al., *Science* **386**, 1243–1250 (2024).
49. J. Manhas, H. I. Edelstein, J. N. Leonard, L. Morsut, *Nat. Chem. Biol.* **18**, 244–255 (2022).
50. X. J. Gao, L. S. Chong, M. S. Kim, M. B. Elowitz, *Science* **361**, 1252–1258 (2018).

ACKNOWLEDGMENTS

We thank members of the Bashor laboratory for helpful discussions. We acknowledge C.-H. Wang for his contributions to development of the modeling framework. We also thank J. Toettcher and S. Boeynaems for advice on engineering and monitoring protein condensates. We thank O. Veiseth and S. Fleury for providing APRE-19 cells. We thank Y. Wang for helping with immunogenicity analysis, R. O'Connell for helping with APRE-19 transfection, and P. Pungchai for assisting with viability analysis. We also thank R. Butcher for setting up the Nikon NASPARC imaging system for taking time-lapse movies. We also thank S. Li and J. Her for helping with cloning. We also thank G. Bedford, J. Li, and I. Hilton for setting up immunoblotting assays.

Funding: This work was supported by grants from NIH R01 EB029483 (C.J.B.), NIH R01 EB032272 (C.J.B.), NIH R21 NS116302 (S.D.O. and C.J.B.), ONR N00014-21-1-4006 (C.J.B.), NIH NIGMS 5R35GM119461 (J.W.R. and P.M.), the Robert J. Kleberg Jr. and Helen C. Kleberg Foundation (C.J.B.), the Claire Glassell Pediatric Fund (S.D.O.), the Grace Reynolds Wall Research Fund (S.D.O.), and NSF GRFP award 1842494 (A.J.W.). **Author contributions:** C.J.B., N.M.D., and X.Y. conceived of the study. C.J.B. and N.M.D. carried out initial experiments. X.Y. built all DNA constructs and carried out experiments to generate the data published herein, with assistance from K.J., A.J.W., J.L., and J.N.; J.W.R., X.Y., K.R., and K.J. developed the quantitative modeling framework, with input and supervision from P.M. and C.J.B.; X.Y. and A.J.W. developed the transwell assay, with supervision from S.D.O. and C.J.B.; K.R. developed image analysis and dynamic circuit

modeling. X.Y., K.R., J.W.R., P.M., and C.J.B. analyzed the data. C.J.B., N.D., and J.J.C supervised the study. X.Y. and C.J.B. wrote the manuscript, with generous input from all authors. **Competing interests:** A provisional patent application that covers technologies described in this manuscript has been filed by Rice University. **Data and code availability:** All data are available in the manuscript or supplementary materials. Sequences of all DNA constructs (table S1) are uploaded to the following Github repository and will be uploaded to Addgene later. All computational data generated in this study and modeling or analysis software code are available at <https://github.com/Emergent-Behaviors-in-Biology/syn-phospho-circuits>. Correspondence and request for materials should be addressed to C.J.B. **License information:** Copyright © 2025 the authors, some rights reserved; exclusive licensee American Association

for the Advancement of Science. No claim to original US government works. <https://www.science.org/about/science-licenses-journal-article-reuse>

SUPPLEMENTARY MATERIALS

science.org/doi/10.1126/science.adm8485
Materials and Methods
Supplementary Text
Figs. S1 to S30
Tables S1 to S6
References (51–157)
Movies S1 and S2

Submitted 9 November 2023; accepted 24 October 2024
10.1126/science.adm8485